LAWRENCE
LIVERMORE
NATIONAL
LABORATORY

LLNL-JRNL-841545

Seismoacoustic Explosion Yield and Depth Estimation: Insights from the Large Surface Explosion Coupling Experiment

K. Kim, M. E. Pasyanos

October 21, 2022

Bulletin of Seismological Society of America

Seismoacoustic Explosion Yield and Depth Estimation: Insights from the Large Surface Explosion Coupling Experiment

Keehoon Kim and Michael E. Pasyanos

Lawrence Livermore National Laboratory, Livermore, CA, USA

Corresponding author: Keehoon Kim (kim84@llnl.gov)

Declaration of Competing Interests

The authors acknowledge there are no conflicts of interest recorded.

Abstract

The Large Surface Explosion Coupling Experiment (LSECE) is a chemical explosion experiment conducted in Yucca Flat at the Nevada National Security Site (NNSS) in 2020. The experiment included two surface detonations of approximately 1000 kg Trinitrotoluene equivalent. The main goal of the experiment was to provide the ground-truth data for seismoacoustic wave excitation by large chemical explosions near the ground surface. The seismic and acoustic energy partitioning between the surface is strongly governed by the depth or height of explosions, and either seismic or acoustic-only analysis may have inherent ambiguity in determining explosion yield and depth simultaneously. Previous studies suggested that joint seismoacoustic analysis can resolve the tradeoff and reduce the uncertainty of yield and depth estimation dramatically. We demonstrate the capability of seismoacoustic analysis to improve the accuracy of explosion yield and depth estimation with the LSECE data. Local acoustic wave propagation in the atmosphere can be substantially affected by constantly varying weather conditions. Consisting of two detonations before dawn and in the afternoon, LSECE provides unique data to evaluate the model accuracy of acoustic wave propagation and seismoacoustic energy partitioning depending on local atmospheric conditions. We quantitatively evaluate the accuracy of yield and depth estimation depending on atmospheric variability and the improvement achieved by the joint seismoacoustic approach.

1. Introduction

Seismology and geophysical acoustics play an important role in explosion monitoring, including event detection and discrimination. The International Monitoring System (IMS) of Comprehensive Nuclear-

Test-Ban Treaty Organization (CTBTO), which is designed to detect any nuclear explosion in the atmosphere, in the oceans, and underground, includes both seismic and acoustic sensors in the network. Determining the yield of explosions and its depth is critical part of the explosion monitoring. In general, seismic and acoustic techniques for the explosion yield estimation have been independently applied, with seismic methods used for deeply-buried explosions and acoustic methods used for near-surface explosions. Because of strong tradeoffs between yield and depth/height, there are large uncertainties in the determination of the explosion yield and depth simultaneously either by seismic or acoustic waves (Ford et al., 2014). This problem is particularly exacerbated for near-surface explosions as small changes of explosion depth and height near the Earth's surface have drastic impact on seismic and acoustic waves amplitudes.

Recently, joint seismoacoustic analysis has received interest for explosion monitoring as an increasing number of regional infrasound (low-frequency acoustic waves) networks effectively complement seismic observations (Arrowsmith et al., 2010; Bonner et al., 2013; Stump et al., 2022). Ford et al. (2014) collected local seismic and overpressure data from the near-surface explosions with various yields and depth-of-burial/height-of-burst and quantitatively determined seismoacoustic energy partitioning depending on their depths, hereafter referred as F14. Although the F14 model provides quantitative predictions for seismic motions and atmospheric pressures near the source, it cannot be applicable to distant observations which are governed by complex propagation path effects. Later, Pasyanos and Ford (2015) used the seismic waveform envelope method (Pasyanos et al., 2012) for near-surface explosions by incorporating F14 in the explosion source model. Seismic wave propagation effects through the media are corrected by accounting for anelastic attenuation and site effects. For acoustic yield estimation, Kim and Rodgers (2016) proposed a similar approach. They accounted for acoustic wave propagation in the atmosphere by using a physics-based propagation simulation and incorporated F14 into the acoustic source model for yield estimation. Pasyanos and Kim (2019) performed joint seismoacoustic analysis for the yield and depth estimation and demonstrated that the joint approach can improve the depth constraint substantially.

Although the seismoacoustic approach showed promising results for simultaneous determination of yield and depth, they might need to be evaluated with more data. The Earth's atmosphere has distinct diurnal variation. On a clear day, the Earth's surface is heated by the sun, and the atmospheric boundary layer (ABL) near the surface has unstable stratification due to buoyancy. Conversely, on a clear night, buoyantly stable stratification is developed in the ABL due to cooling of the ground. Although this diurnal change of near-surface atmosphere is not critical to seismic waves in the solid Earth, acoustic wave generation and propagation by near-surface explosions can be substantially affected (Wilson et al., 2015). Many empirical models were developed to address explosion-generated acoustic waves. However, those models were generally determined by the limited data collected from explosion experiments in the daytime, and it is possible that those acoustic data were biased by the characteristic stratification of atmosphere in daytime. Although acoustic wave propagation in nighttime has been reported and investigated before (Fee and Garces, 2007; Blom and Waxler, 2012), the ground-truth data measured from known sources and quantitative analysis are rare for yield estimation.

In this study, we evaluate the seismoacoustic yield estimation technique with unique seismic and acoustic data obtained from the comparison of two surface explosions at different times of a day. This chemical explosion experiment, called the Large Surface Explosion Coupling Experiment (LSECE), includes a detonation at the dawn before the ABL develops unstable stratification and provides a unique dataset to characterize acoustic wave propagation in this atmospheric condition. We focus on acoustic signal analysis, which strongly depends on atmospheric conditions, and quantitatively compare the acoustic signals with existing dataset obtained in daytime. This analysis provides a rare opportunity to evaluate the empirical model developed from the data in daytime. Finally, we extend the analysis for seismoacoustic yield estimation by incorporating seismic data and analyze the uncertainty of yield estimates due to the characteristic weather conditions at the dawn.

2. Data

LSECE is a chemical explosion experiment conducted in Yucca Flat at the Nevada National Security Site (NNSS) in October 2020. The main goal of the experiment was to provide the ground-truth data for acoustic and seismic wave coupling generated by large chemical explosions (Vorobiev and Ford, 2022). The experiment consisted of two surface explosions of 992.05 and 991.5 kg Trinitrotoluene (TNT) equivalent. The first shot (LSECE-1) was conducted on 27 October 2020 at 6:37 am local time (13:37 UTC) before the sunrise in Nevada. The second shot (LSECE-2) was conducted on 29 October at 3:35 pm local time (22:35 UTC) during the daytime. The atmospheric temperature profiles in the ABL were distinctly different due to the shot time, and the experiment produced a unique dataset to exhibit the sensitivity of acoustic wave excitation and propagation in the different weather conditions. The geology of the test site in this region is characterized by alluvium layers which can affect the seismoacoustic partitioning between the atmosphere and subsurface. The LSECE experiment took place at the same location of the Source Physics Experiment (SPE) Phase II in Dry Alluvium Geology (DAG) which consisted of four buried explosions (Berg and Poppeliers, 2022). Hence, the LSECE seismic and acoustic signals in addition to the SPE DAG provide the ground truth data to understand seismoacoustic energy partitioning for surface and buried explosions across dry alluvium.

LSECE included 30 overpressure sensors deployed near the source for non-linear blast measurements (Vorobiev and Ford, 2022) and 54 acoustic/infrasonic sensors located between 1 to 9 km from the source. In this study, we used the linear infrasound array with 12 sensors deployed in the north-south direction for yield estimation (Figure 1). This linear array captured gradual waveform evolution depending on propagation distances, which is suitable for quantitative analysis of excited acoustic energy and its propagation near the ground. These stations consisted of a single Hyperion IFS5000 sensor with a flat frequency response between 0.01 – 100 Hz.

Local weather conditions were also measured by launching a radiosonde before the detonations. Figure 2 shows background temperatures, and meridional (northerly) wind profiles obtained by the radiosonde sounding. Both temperature and meridional winds affect the local acoustic propagation by contributing to effective sound speed profiles in air. The two temperature profiles measured before the dawn and in the daytime show drastically different gradients with respect to the elevation. Atmospheric temperature gradients are generally negative in the daytime due to higher temperature of the ground surface, which leads to negative sound speed gradient with respect to increasing elevation (Wilson et al., 2015). In the negative sound speed gradient, acoustic waves near the ground refract upward and result in reduced amplitudes near the ground (Rayleigh, 1896; Kim and Rodgers, 2017). Conversely, positive or neutral gradient of sound speeds can be produced before the dawn, and acoustic wave amplitudes increase near the ground by enhancing downward refraction or suppressing upward refraction (Blom and Waxler, 2012).

The impact of different temperature profiles is observed in the LSECE data. Figure 3 shows the peak overpressures measurements for LSECE-1 (blue circles) and 2 (green). The peak overpressures and observation distances are scaled for 1kg TNT explosion and compared with the other dataset (gray circles) which were collected from previous explosion experiments in daytime. These data were used by Schnurr et al. (2020) to develop the average peak overpressure model (denoted by red line) and its statistical variation (red vertical error bars). A semi-empirical model developed for a homogeneous atmosphere (KG85) is also shown as a black line (Kinney and Graham, 1985). The peak overpressure amplitudes for LSECE-2 suffer larger attenuation than the homogeneous KG85 model as the propagation distance increases. This is attributed to the negative temperature gradient leading to upward refraction of acoustic waves near the ground. This attenuation rate for LSECE-2 follows almost exactly the mean model of previous dataset as they have similar sound speed structures in daytime. However, the peak amplitudes for LSECE-1 have larger than the mean model over one standard-deviation amplitude, indicating the LSECE-1 amplitudes are significantly different from those observed in daytime. These higher amplitudes are attributed to the combination of atmospheric temperature and wind conditions. During LSECE-1, the background temperature profile showed a very weak gradient against elevations, which would not cause effective upward refraction of sound. In addition, strong wind jet from north to south was observed at 1 km above the ground (Figure 2). The effective sound speed profile is determined by the wind speed added to the sound speed of air (Figure 2), and this strong wind at 1 km altitude created an effective waveguide below. Propagating acoustic waves near the ground is trapped in this waveguide, and their amplitudes undergo less attenuation or even increase at certain distances due to downward refraction. The LSECE data indicate that this characteristic sound speed structures observed before the dawn have great impact on the local acoustic wave propagation, and the existing data and model obtained from daytime explosions cannot account for the observations for LSECE-1.

The explosions were well-recorded by dozens of stations at local distance. For our analysis, however, we preferentially select stations close enough to have good signal-to-noise, but distant enough for the coda to be well-formed. We also want to use a station which has been calibrated for local site effects using earthquakes. For the seismic yield analysis, we use station TPNV (Topopah Spring, NV), a long running and well-calibrated station in the U.S. National Seismic Network located 24 km southwest of ground zero. In contrast to the acoustic signal, the seismic waves from the two explosions were very similar, despite the presence of a crater created by the first shot for the second one. Figure 4 shows the seismic signals of the two explosions. We observe significantly larger ground-coupled acoustic waves for the first explosion (in red) at TPNV than the second explosion (in blue). While the two seismic signals are nearly identical, there are some small differences in the pre-event noise and the coda, which is reflected in small differences in the coda envelopes.

3. Acoustic Yield Estimation

3.1. Acoustic Inversion

We perform the acoustic yield estimation based on a Bayesian approach (Modrak et al., 2010; Blom et al., 2018; Kim et al., 2021). The posterior distribution of yields (*P(W|E)*) at the given data (*E*) is written as follows.

$$P(W|E) = \frac{P(E|W)P(W)}{c} \quad (1)$$

The probability distribution of yield is determined based on the likelihood of acoustic energy (*E*) at a given yield (*W*), and the normalization constant of the distribution is denoted by *c*. *P(W)* is the prior distribution of yields and assumed to be uniform in this study. The likelihood *P(E|W)* is assumed Gaussian distribution as

$$P(E|W) = \frac{1}{\sqrt{2\pi\sigma^2}} exp \frac{-1}{2}\left(\frac{E_p(W)-E(W)}{\sigma}\right)^2, \quad (2)$$

The variance (σ^2) governs the uncertainty of the yield estimate *P(W|E)*. In this study, we determined the variance of acoustic energy from the other dataset obtained by various explosions. This will be discussed in Section 3.3.

We measure the acoustic energy (E) in the frequency domain between a frequency f_1 and f_2. The predicted acoustic energy (Ep) is measured from the predicted spectrum as

$$E_p(W,x) = \int_{f_1}^{f_2} \parallel S(w,f,x_0)T(f,x;x_0) \parallel^2 df. \quad (3)$$

We predict acoustic spectrum by multiplying acoustic source spectrum ($S(W, f, x_0)$) at a position x_0 by the transmission loss (T) from x_0 to x. There may be various ways to calculate the transmission loss. In this study, we used physics-based numerical simulations to obtain the transmission loss and explained the processes in Section 3.2. The source model for the acoustic source spectrum is also discussed in Section 3.3.

3.2. Acoustic Propagation Simulations

The accuracy of yield estimation in Equation 1 strongly depends on the accurate calculation of the transmission loss in Equation 3. It has been reported that local acoustic wave propagation can have large variations depending on the weather conditions in the ABL (Fee and Garces, 2007; Blom and Waxler, 2012; Kim and Rodgers, 2017; Kim et al., 2018). Our data from LSECE-1and 2 also demonstrate that an empirical model determined in a certain weather condition may not account for the amplitude variations in different conditions. In this study, we perform a physics-based numerical simulation to account for the acoustic wave propagation and amplitude variation due to the weather variability. We use the finite-difference code, ElAc, to calculate numerical Green's functions from the source to the receivers. ElAc is a seismoacoustic code developed by Lawrence Livermore National Laboratory (Petersson and Sjogreen, 2018) and used for full-waveform simulation of acoustic waves in the atmosphere (Kim and Rodgers, 2017; Kim et al., 2018). ElAc solves the Linearized Euler Equation in the atmosphere with 6th order finite-difference scheme which satisfies the summation-by-parts principle and guarantees the stability of solutions (Strand, 1994). It also adopts curvilinear grids following surface topography. This terrain-following grid defines smooth surface boundary removing artificial scattering of waves due to the staircase approximation of interface boundary in rectangular grids.

The numerical simulations are performed in the spatial domain over 20 km in the north-south and 7 km in the east-west direction. The vertical extent of the domain is 4 km above the ground. The ground surface elevation (Figure 1) is specified by the US national digital elevation model with a 10 m spatial resolution. The grid spacing of finite-difference stencil is 3 m which satisfies the requirement of eight grid points per wavelengths and minimize artificial dispersion up to 10 Hz. For numerical source time functions, we used a Gaussian-type function with a corner frequency of 10 Hz. The numerical Green's functions with this configuration are valid up to 10 Hz, providing the transmission loss in Equation 3.

The background condition of atmosphere for the simulation is specified by the local radiosonde sounding data. The temperature, wind, and pressure profiles obtained before the shots were used for the simulations. Since we have only one profile at a single position, the atmosphere is defined as 1-D, horizontally stratified layers. Although the Earth's atmosphere is generally characterized by stratified layers due to the gravity, the ABL near the ground can be highly turbulent by diurnal heating/cooling and complex topography of the ground (Kim et al., 2018). In that case, the 1-D atmosphere model in the simulations may underestimate the lateral variability of the ABL and produce large prediction errors for wave amplitudes.

The modeling results are shown in Figure 5 for LSECE-1. The images of acoustic wave propagation are captured in a vertical cross-section in the north-south direction from the source. In the beginning of simulations, the acoustic waves propagate spherically near the source, but the overall wavefront starts undergoing distortion by the atmospheric sound speed structure at further distances. As we expected from the temperature and wind profiles in Figure 2, the acoustic waves are trapped in the waveguide below 1km to the south, and their amplitudes are much larger than waves traveling to the north. This is due to the directional wind. The strong wind to the south created the waveguide but reduced the effective sound speed gradient to the north, resulting in lower amplitudes in the north direction.

Figure 6 and 7 show the quantitative comparison of numerical simulation and observations for LSECE-1. Figure 6 compares the observed signal at 1 km south from the source with the numerical simulation results and empirical model. The waveform data and predicted models are aligned with respect to their peak amplitudes for relative amplitude comparison. The empirical waveform was obtained from the acoustic source model proposed by Kim et al (2021), hereafter called K21. The K21 model was scaled for 992 kg TNT explosion, and the amplitude attenuation to the observation distance was calculated by the geometric spreading (inversely proportional to the distance) in a homogeneous atmosphere. At the relatively close distance from the source, both the empirical and finite-difference models show good agreement with the observations indicating that the propagation effects due to atmospheric variation are not significant. However, the predictions from the two models are completely different at the distance of 7 km in Figure 7. The observed amplitudes are considerably larger than the prediction by the homogeneous K21 model. The observed acoustic signals are enhanced by the waveguide near the ground, but the empirical model with a homogeneous atmosphere cannot account for this effect and results in significantly underestimated amplitudes at 7 km. However, the finite-difference model takes into account the sound speed profile near the ground and predicted comparable amplitudes to the observation. These apparent acoustic source model and linear propagation simulation are intended to predict acoustic energy attenuation in the far field out of the nonlinear shock regime (Kim et al., 2021; Kim and Pasyanos, 2022). The linear acoustic modeling may not be suitable for the prediction of signal arrival time in the local distances as the blast waves propagate faster than the speed of sound near the source.

Figure 8 and 9 compare the signals for LSECE-2. As for Figure 6, the observation signal at 1 km south shows good agreement with either empirical or numerical model for LSECE-2. The empirical models for LSECE-1 and 2 indicate that the weather condition is not critical to the acoustic amplitude variation at the close distance, and the homogeneous atmosphere model can be used for the prediction regardless of weather conditions. However, at 7 km from the source in Figure 9, the empirical model substantially overestimated acoustic amplitudes due to unaccounted upward refraction in the negative temperature gradient and may not be suitable for relatively long-distance propagation. The finite-difference simulation still shows good agreement with the observations as in LSECE-1. As long as appropriate weather profiles are used, the physics-based numerical modeling seems to have the capability to account for acoustic wave propagation near the ground.

3.3. Yield Estimate for Surface Explosions

The yield estimation based on Equation 3 requires the acoustic source spectrum and transmission loss calculation for acoustic energy radiation. We used the K21 model to obtain acoustic source spectra for arbitrary yields. The K21 model was empirically developed by surface explosion data and can be directly used for yield estimation of surface explosions like LSECE. Based on the scaling law of blast waves (Kinney and Graham, 1985) and regression analysis of the data, the standard waveform (*p(t)*) for a 1kg TNT explosion at the surface was determined in K21. This waveform represents apparent acoustic pressures recorded at 1m from the source and is defined by the analytic functions as

$$p(t) = \begin{cases} p_p\left(1-\frac{t}{t_p}\right), 0 \le \frac{t}{t_p} \le 1, \\ p_p\frac{1}{6}\left(1-\frac{t}{t_p}\right)\left(1+\sqrt{6}-\frac{t}{t_p}\right)^2, 1 < \frac{t}{t_p} \le 1+\sqrt{6}. \end{cases} \quad (4)$$

Based on the statistical properties of the data, the probability distribution of the peak pressure (p_p) and positive period (t_p) is also expressed in the bivariate normal distribution (ρ),

$$\rho(p_p, t_p) = \frac{1}{2\pi\delta_p\delta_t\sqrt{1-c^2}} exp\left\{\frac{-1}{2(1-c^2)}\left(\frac{\left(p_p-\overline{p}_p\right)^2}{\delta_p^2} + \frac{\left(t_p-\overline{t}_p\right)^2}{\delta_t^2} - 2c\frac{\left(p_p-\overline{p}_p\right)\left(t_p-\overline{t}_p\right)}{\delta_p^2\delta_t^2}\right)\right\}, \quad (5)$$

where $\overline{p}_p$= 86,900 Pa and $\overline{t}_p$=5.08×10^{-3} s. δ_p^2 and δ_t^2 are the variances of p_p and t_p, respectively, and *c* is the covariance shown in the Table 2 in Kim et al. (2021). From Equation 4 and 5, acoustic source waveforms for 1kg TNT explosion are calculated and scaled for arbitrary yields following the scaling law as

$$\hat{p}_p(W) = p_p \frac{P_a}{P_0}\left(\frac{\alpha W^{\frac{1}{3}}}{f_d}\right), \quad (6)$$

$$\hat{t}_p(W) = t_p\left(\frac{\alpha W^{\frac{1}{3}}}{f_t}\right), \quad (7)$$

$$f_d = \left(\frac{P_a}{P_0}\right)^{1/3}\left(\frac{T_a}{T_0}\right)^{-1/3}, \quad (8)$$

$$f_t = \left(\frac{P_a}{P_0}\right)^{1/3}\left(\frac{T_a}{T_0}\right)^{1/6}, \quad (9)$$

where $\hat{p}_p$ and $\hat{t}_p$ are peak pressure and positive period for arbitrary yields W. The atmospheric correction factors f_d and f_t are obtained by the atmosphere temperature (T_a) and ambient pressure (P_a) in comparison with the reference P_0=101,325 Pa and T_0= 288.15 K. Note that the effective yield is determined by the effectiveness factor (α). In this study, the effectiveness factor was assumed 2 as the ground surface effectively doubles the acoustic energy for surface explosions (Kinney and Graham, 1985; Kim and Rodgers 2016).

Figure 10 shows the process to predict the acoustic spectrum. First, we generated 500 random realizations of source spectra at a given yield based on the probability distribution of the K21 model. Transmission losses are calculated by dividing synthetic Green's function for each station by the Green's functions at 1m from the source. The prediction at the observing station is made by multiplying the source spectrum and transmission loss in the frequency domain (described in Equation 3). Finally, the acoustic energies for the observations and predictions are measured between 1 – 10 Hz following Equation 3 and compared for different yields between 1 kg and 20 metric tons. We observed the peak frequency near 5 Hz in the recorded signals, and the frequency range for acoustic energy calculation includes the majority of observed energies. In addition, our finite-difference setup supports stable simulations up to 10 Hz. Due to the range of predictions made by the source model, the variance of acoustic energies in Equation 2 is directly calculated from the set of predictions. This variance of prediction depends on the variance of source model as the transmission loss is not a random variable in our approach. However, the variance of the K21 model was determined by local acoustic observation from various yields and distances, and thus, represents possible variability of local acoustic amplitudes.

Figure 11 and 12 show estimated yields and their probability distribution for LSECE-1 and 2 based on Equation 1 and 2. We calculate the probability distributions for 8 stations located between 5.5 – 8 km from the source and combined them for the joint distribution. The stations within a 5 km distance may be able to improve the accuracy of estimated yields. However, they are generally independent to weather conditions as shown in Figure 6 and 8 and not suitable for evaluating the yield estimation capability in different weather conditions. For LSECE-1, the maximum likelihood yield estimate is 1287 kg for explosion at surface. The 99% confident interval is between 963 – 1920 kg showing acceptable ranges. LSECE-2 shows the estimate yield of 550 kg at the maximum likelihood and the 99% confidence interval between 420 – 781 kg. This yield is considered significantly underestimated as the nominal yield falls out of the confident range. This large error for yield estimation seems to be caused by the propagation prediction errors due to the poor resolution of atmospheric specification. In this study, we assumed 1-D stratified atmosphere due to limited atmospheric data. However, the 1-D model may not represent the lateral variability of the ABL resulting in large prediction error (Kim et al., 2018).

Although the propagation simulation and estimated yields strongly depend on the accuracy and resolution of weather specification, our approach using the physics-based propagation model showed significantly improved results than those by the homogeneous K21 model. Figure 13 and 14 show the estimated yield by those two prediction models. The homogeneous model estimates the yields of 3464 kg for LSECE-1 and 308 kg for LSECE-2, which have unacceptably large error. In contrast to the homogeneous model, the finite-difference simulation results in more reasonable estimation error. Higher-resolution weather specification should be the key to improve the accuracy of yield estimates in our approach.

4. Seismoacoustic Approach for Yield and Depth Estimation

4.1. Acoustic Likelihood

Although the K21 model provides full waveform information of explosion-generated acoustic waves and can be used for a source model in Equation (3), it was developed based on only surface explosions and cannot be applied for explosions at arbitrary depth or height near the ground. In this section, we explore the explosion blast model developed by Ford et al. (2014, 2021) for simultaneous yield and depth estimation for acoustic waves. By using a series of low-yield near-surface chemical explosion experiments, Ford et al. (2021) developed an empirical model which provides acoustic pressure and seismic motion prediction at a given yield and depth/height. The Ford's model for soft-rock (e.g., alluvium) defines atmospheric overpressure impulse (i_s) as

$$ln(i_s) = \beta_1 + \beta_2 ln(r_s) + \beta_3 h_s - ln[1 + exp(\beta_3 h_s)], \quad (10)$$
$$\beta_1 = 6.16, \beta_2 = -1.14, \beta_3 = 5.06,$$

where the scaled impulse (i_s), scaled range (r_s) and the scale height-of-burst (h_s) are the quantities scaled for a 1kg TNT explosion. Equation (10) calculates overpressure impulses which depend on not only the source size (W) and depth (h_s) but also the propagation distance (r_s). Later, Kim and Rodgers (2016) defined the reduced acoustic impulse from Equation (10). Unlike the acoustic impulses in Equation (10), the reduced acoustic impulse is a source property depending only on the size of source representing apparent impulse at 1m from the explosion and defined as

$$I_{1kg} = 2\pi r_s i_s(r_s), \quad (11)$$

where I_{1kg} is the reduced acoustic impulse for 1kg TNT explosion, $r_s = 20$m, 2π is a geometric spreading factor in a halfspace. The reduced acoustic impulse for arbitrary yields can be obtained by the scaling law as

$$I_W(W) = I_{1kg} f_t W^{2/3}, \quad (12)$$

where f_t is the atmosphere correction factor in Equation (9). We explore the variation of the reduced acoustic impulse in a range of depths and yields and define the likelihood function with a normal distribution assumption as

$$L(I_w) = \frac{1}{\delta_I \sqrt{2\pi}} exp\left[\frac{-1}{2} \frac{\left(I_W(W,h) - I_0\right)^2}{\delta_I^2}\right], \quad (13)$$

whereI_0 and $\delta_I^2$is the reduced acoustic impulse and its variance for a surface explosion of 1287 kg for LSECE-1 and 550 kg for LSECE-2 (the estimated yield from the waveform inversion in this study). We calculated the variance of acoustic impulse (δ_I^2) from the acoustic impulses derived from the probability distribution for the surface explosions in Figure 11 and 12. Instead of individual distribution for each station, the final joint distributions for LSECE-1 and 2 are used to obtain the acoustic impulse distributions and their variances (δ_I^2).

4.2. Seismic Likelihood

Seismic yields are estimated using the regional waveform envelope yield method, first described in Pasyanos et al., (2012), which couples an explosion source with models to account for the propagation. In terms of specifics, we use the explosion source model of Walter and Ford (2018), where the propagation consists of calibrated coda shapes and Q with accompanying station site terms from an updated attenuation model for the United States (Pasyanos, 2013). The method, initially developed for underground events, was extended to near-surface explosions in Pasyanos and Ford (2015) by using an energy-partitioning model (F14). The material properties for the explosion source are taken from the measured parameters of the shallowest SPE DAG explosion (DAG-4): Vp=1416 m/s, Vs=805 m/s, 1913 kg/m^3, and gas porosity of 27.5%. Envelopes from station TPNV between 4 and 10 Hz (4-6, 6-8, and 8-10 Hz) are used in the analysis. We test yields ranging from 1 kg to 100 t TNT-equivalent and from heights of 10 m to depths of 10 m. As expected from the coupling codes, there is a tradeoff between yield and depth, with a larger yield required for above surface events and a smaller yield for fully buried explosions. We find a minimum misfit of 1.0 tons and 1.5 tons at the surface for LSECE-1 and 2, respectively. Uncertainties, which are used to transform misfit into likelihood, are derived from uncertainties from the regressions in the surface coupling model (F14). These uncertainties could potentially be reduced by new regressions and additional modeling for a variety of material conditions.

4.2. Joint Likelihood

We follow the joint likelihood method for seismoacoustic yield estimation suggested by Pasyanos and Kim (2019). Assuming the seismic and acoustic observations are independent, the joint likelihood function (L) for yields can be constructed by the multiplication of the independent seismic and acoustic likelihoods as

$$L_{yield} = L_{acoustic} \text{ x } L_{seismic}.$$

The combined likelihoods are shown in Figure 15 and 16. The likelihood functions are computed for the yields between 0.001 – 100 tons and depths between -10 – 10 m, and their cumulative likelihoods over the interval are normalized to unity. In general, individual likelihood from seismic and acoustic analysis has a strong trade-off between explosion yield and depth. The region with high likelihood values stretches over a wide range of depths, and it is difficult to determine a reliable depth based on either individual seismic or acoustic likelihoods. However, by combining the two likelihoods, the constraints for depths are significantly improved. Without any priori for the depth and yield, the maximum likelihood depths for LSECE-1 and 2 are estimated at -0.99 and 1.25 m, respectively, indicating near-surface explosions. The yields are also estimated as 1.0 ton for LSECE-1 and 2, which are improved from individual estimates. In addition, the shape of likelihoods is a well-defined ellipse, allowing for the reliable determination of yield and depth simultaneously. This improvement was achieved by the different sensitivities of seismic and acoustic signals to the depth of explosions.

The uncertainties of combined likelihoods are also affected by the individual likelihoods. The variance of yields in the acoustic likelihoods appears smaller than that in seismic likelihoods for both LSECE-1 and 2. This observation may reflect the fact that sound speed structures of the atmosphere are relatively simpler than the subsurface seismic velocities at the considered wavelengths and results in less variability of acoustic signals. The small variance of acoustic likelihood significantly reduced the uncertainty of joint likelihood. This suggests that either more accurate seismic or acoustic likelihood can complement the other to improve the accuracy of resultant yield and depth estimates.

5. Conclusion

We investigated the capability of seismoacoustic yield estimation for chemical explosions in different meteorological conditions. The LSECE experiment with two surface detonations before dawn and in the afternoon provided the rare ground-truth data for seismic and acoustic signal generation and propagation. The data showed that the excitation of seismic and acoustic energy is consistent but acoustic propagation is significantly affected by the variation of atmospheric boundary layer near the ground. Without accounting for this atmospheric propagation-path effect, the yield estimation by the acoustic-only signals would have unacceptably large uncertainty. Individual seismic and acoustic yield estimation showed large uncertainty for depth determination. However, by combining seismic and acoustic likelihoods, the depth constraint was significantly improved, allowing for reliable determination of both depth and yield. Our analysis also showed the seismic and acoustic likelihoods effectively complement each other to not only improve the accuracy of yield and depth but also reduce the uncertainty of the estimates.

Data and Resources

Data collected as part of LSECE are under a two-year embargo and is anticipated to be available to the public at the IRIS Data Center (www.iris.edu) starting in October 2022. Seismic data from TPNV is part of the U.S. National Seismic Network (https://doi.org/10.7914/SN/US) and data is available at the IRIS Data Center.

Acknowledgments

The Large Surface Explosion Coupling Experiment (LSECE) would not have been possible without the support of many people from several organizations. The authors wish to express our gratitude to the LSECE working group and multi-institutional and interdisciplinary group of scientists and engineers for the field experiment. The authors also thank two anonymous reviewers for their valuable feedback that improved the article. The experiment and follow-on research was supported by the Nuclear Arms Control Technology (NACT) program at the Defense Threat Reduction Agency (DTRA). The views expressed in the article do not necessarily represent the views of the U.S. Department of Energy or the U.S. Government. This work was performed under the auspices of the U.S. Department of Energy by the Lawrence Livermore National Laboratory under Contract Number DE-AC52-07NA27344. This is LLNL Contribution LLNL-JRNL-841545.

References

Arrowsmith, S. J., Johnson, J. B., Drob, D. P., & Hedlin, M. A. (2010). The seismoacoustic wavefield: A new paradigm in studying geophysical phenomena. *Reviews of Geophysics*, *48*(4), doi:10.1029/2010RG000335

Berg, E. M., & Poppeliers, C. (2022). Inversion of Infrasound Time Series for Seismoacoustic Source Parameters Produced by a Buried Chemical Explosion at the Source Physics Experiment Phase II: Dry Alluvium Geology. *Bulletin of the Seismological Society of America*, *112*(4), 2216-2230, doi:10.1785/0120220020

Blom, P., & Waxler, R. (2012). Impulse propagation in the nocturnal boundary layer: Analysis of the geometric component. *The Journal of the Acoustical Society of America*, *131*(5), 3680-3690, doi:10.1121/1.3699174

Blom, P. S., Dannemann, F. K., & Marcillo, O. E. (2018). Bayesian characterization of explosive sources using infrasonic signals. *Geophysical Journal International*, *215*(1), 240-251, doi:10.1093/gji/ggy258

Bonner, J., Waxler, R., Gitterman, Y., & Hofstetter, R. (2013). Seismo-acoustic energy partitioning at near-source and local distances from the 2011 Sayarim explosions in the Negev Desert, Israel. *Bulletin of the Seismological Society of America*, *103*(2A), 741-758, doi:10.1785/0120120181

Fee, D., & Garcés, M. (2007). Infrasonic tremor in the diffraction zone. *Geophysical Research Letters*, *34*(16), doi:10.1029/2007GL030616

Ford, S. R., Rodgers, A. J., Xu, H., Templeton, D. C., Harben, P., Foxall, W., & Reinke, R. E. (2014). Partitioning of seismoacoustic energy and estimation of yield and height-of-burst/depth-of-burial for near-surface explosions. *Bulletin of the Seismological Society of America*, *104*(2), 608-623, doi:10.1785/0120130130

Ford, S. R., Bulaevskaya, V., Ramirez, A., Johannesson, G., & Rodgers, A. J. (2021). Joint Bayesian inference for near-surface explosion yield and height-of-burst. *Journal of Geophysical Research: Solid Earth*, 126, e2020JB020968. https://doi.org/10.1029/2020JB020968

Kim, K., & Rodgers, A. (2016). Waveform inversion of acoustic waves for explosion yield estimation. *Geophysical Research Letters*, *43*(13), 6883-6890, doi:10.1002/2016GL069624

Kim, K., & Rodgers, A. (2017). Influence of low-altitude meteorological conditions on local infrasound propagation investigated by 3-D full-waveform modeling. *Geophysical Journal International*, *210*(2), 1252-1263, doi:10.1093/gji/ggx218

Kim, K., Rodgers, A., & Seastrand, D. (2018). Local infrasound variability related to in situ atmospheric observation. *Geophysical Research Letters*, *45*(7), 2954-2962, doi:10.1002/2018GL077124

Kim, K., Rodgers, A. R., Garces, M. A., & Myers, S. C. (2021). Empirical acoustic source model for chemical explosions in air. *Bulletin of the Seismological Society of America*, *111*(5), 2862-2880, doi.org/10.1785/0120210030

Kim, K., & Pasyanos, M. E. (2022). Yield Estimation of the August 2020 Beirut Explosion by Using Physics-Based Propagation Simulations of Regional Infrasound. *Geophysical Research Letters*, e2022GL101118, https://doi.org/10.1029/2022GL101118.

Kinney, G. & Graham, K., (1985). Explosive Shocks in Air, Springer-Verlag, 282 pp.

Modrak, R. T., Arrowsmith, S. J., & Anderson, D. N. (2010). A Bayesian framework for infrasound location. *Geophysical Journal International*, *181*(1), 399-405, doi:10.1111/j.1365-246X.2010.04499.x

Pasyanos, M. E., Walter, W. R., & Mayeda, K. M. (2012). Exploiting regional amplitude envelopes: A case study for earthquakes and explosions in the Korean Peninsula. *Bulletin of the Seismological Society of America*, *102*(5), 1938-1948, doi: 10.1785/0120120012.

Pasyanos, M.E. (2013). A lithospheric attenuation model of North America, *Bulletin of the Seismological Society of America*, 103, 3321-3333, doi: 10.1093/0120130122.

Pasyanos, M. E., & Ford, S. R. (2015). Determining the source characteristics of explosions near the Earth's surface. *Geophysical Research Letters*, *42*(10), 3786-3792, doi: 10.1002/2015GL063624.

Pasyanos, M. E., & Kim, K. (2019). Seismoacoustic analysis of chemical explosions at the Nevada National Security Site. *Journal of Geophysical Research: Solid Earth*, *124*(1), 908-924, doi: 10.1029/2018JB016705.

Petersson, N. A., & Sjögreen, B. (2018). High order accurate finite difference modeling of seismo-acoustic wave propagation in a moving atmosphere and a heterogeneous earth model coupled across a realistic topography. *Journal of Scientific Computing*, *74*(1), 290-323, doi:10.1007/s10915-017-0434-7

Rayleigh, J. W. S. B. (1896), The Theory of Sound, vol.2, Dover, NewYork

Schnurr, J., Kim, K., Garces, M. A., & Rodgers, A. (2020). Improved parametric models for explosion pressure signals derived from large datasets. *Seismological Research Letters*, *91*(3), 1752-1762, doi:10.1785/0220190278

Strand, B. (1994). Summation by parts for finite difference approximations for d/dx. *Journal of Computational Physics*, *110*(1), 47-67, doi:10.1006/jcph.1994.1005

Stump, B., Hayward, C., Golden, P., Park, J., Kubacki, R., Cain, C., ... & Jun, M. S. (2022). Seismic and Infrasound Data Recorded at Regional Seismoacoustic Research Arrays in South Korea from the Six DPRK Underground Nuclear Explosions. *Seismological Society of America*, *93*(4), 2389-2400, doi:10.1785/0220220009

Vorobiev, O. Y. and S. R. Ford (2022). Airblast observations and near-field modeling of the Large Surface Explosion Coupling Experiment (LSECE), submitted to and under review in *Shock Waves.*

Walter, W.R. and S.R. Ford (2018). A preliminary explosion seismic spectral model for saturated/hard rock, Lawrence Livermore National Laboratory, LLNL-TR-754292, 14 pp., doi:10.2172/1460932.

Wilson, D. K., Pettit, C. L., & Ostashev, V. E. (2015). *Sound propagation in the atmospheric boundary layer*. Acoustical Society of America.

Keehoon Kim
kim84@llnl.gov
7000 East Avenue,
Livermore, CA 94550

Michael E. Pasyanos
pasyanos1@llnl.gov
7000 East Avenue,
Livermore, CA 94550

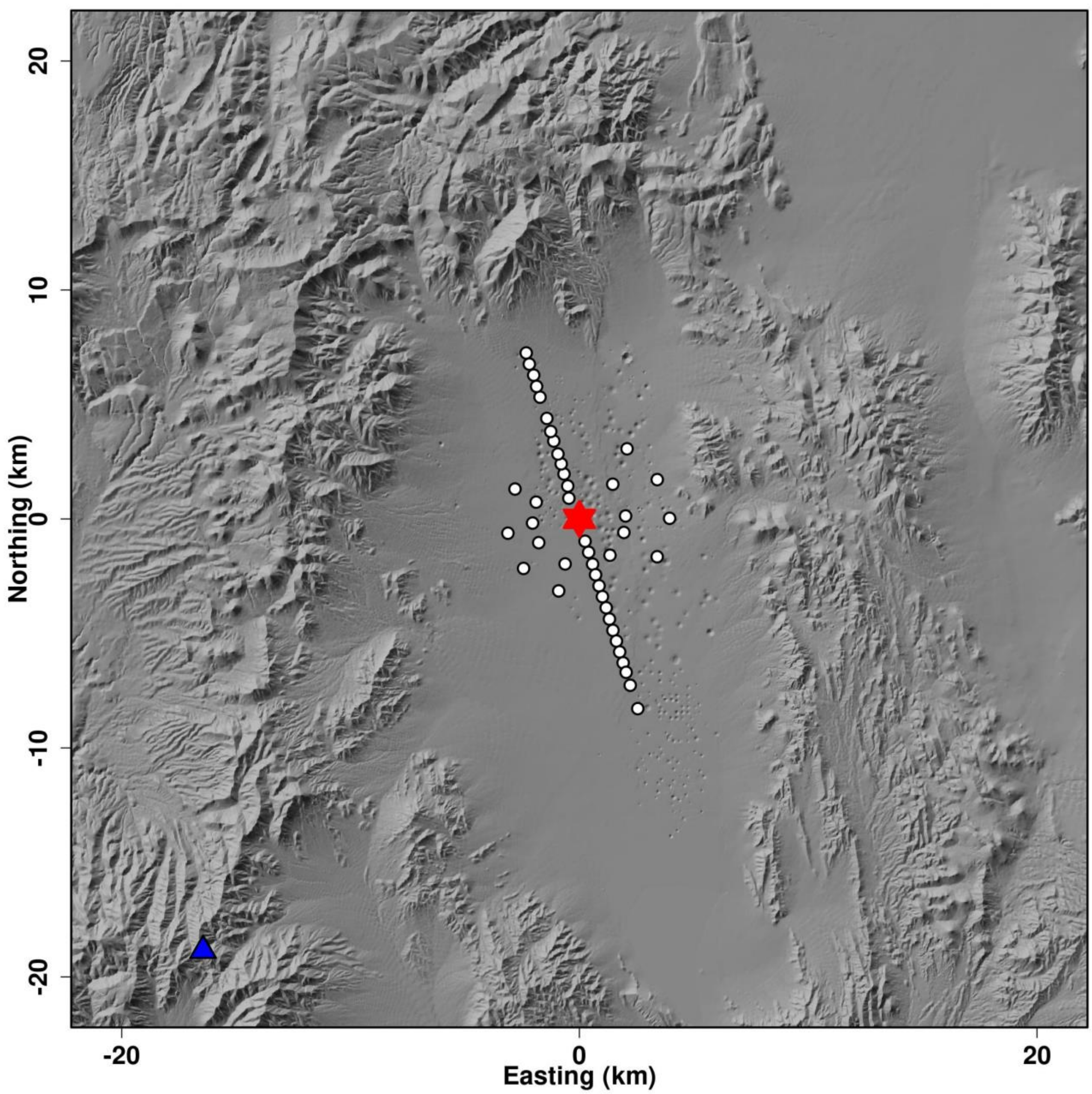

Figure 1. The acoustic sensor network (white circles) deployed for the LSECE experiment. Ground zero is denoted by the red star, and the seismic station (TPNV) used for the analysis is indicated by the blue triangle.

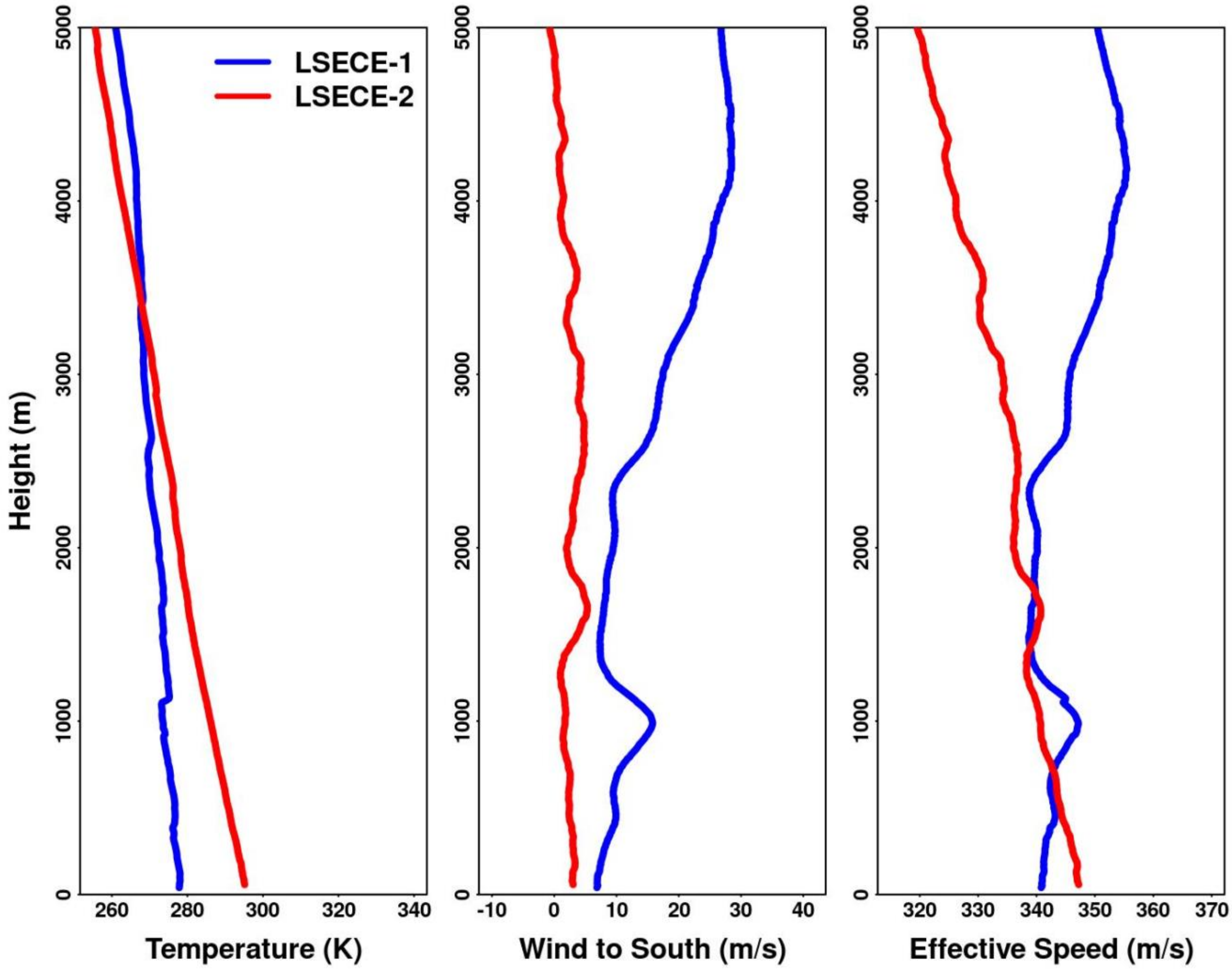

Figure 2. Atmospheric temperature and meridional wind profiles measured by local radiosonde sounding. The effective sound speed profiles to the south were computed from the temperature and wind data.

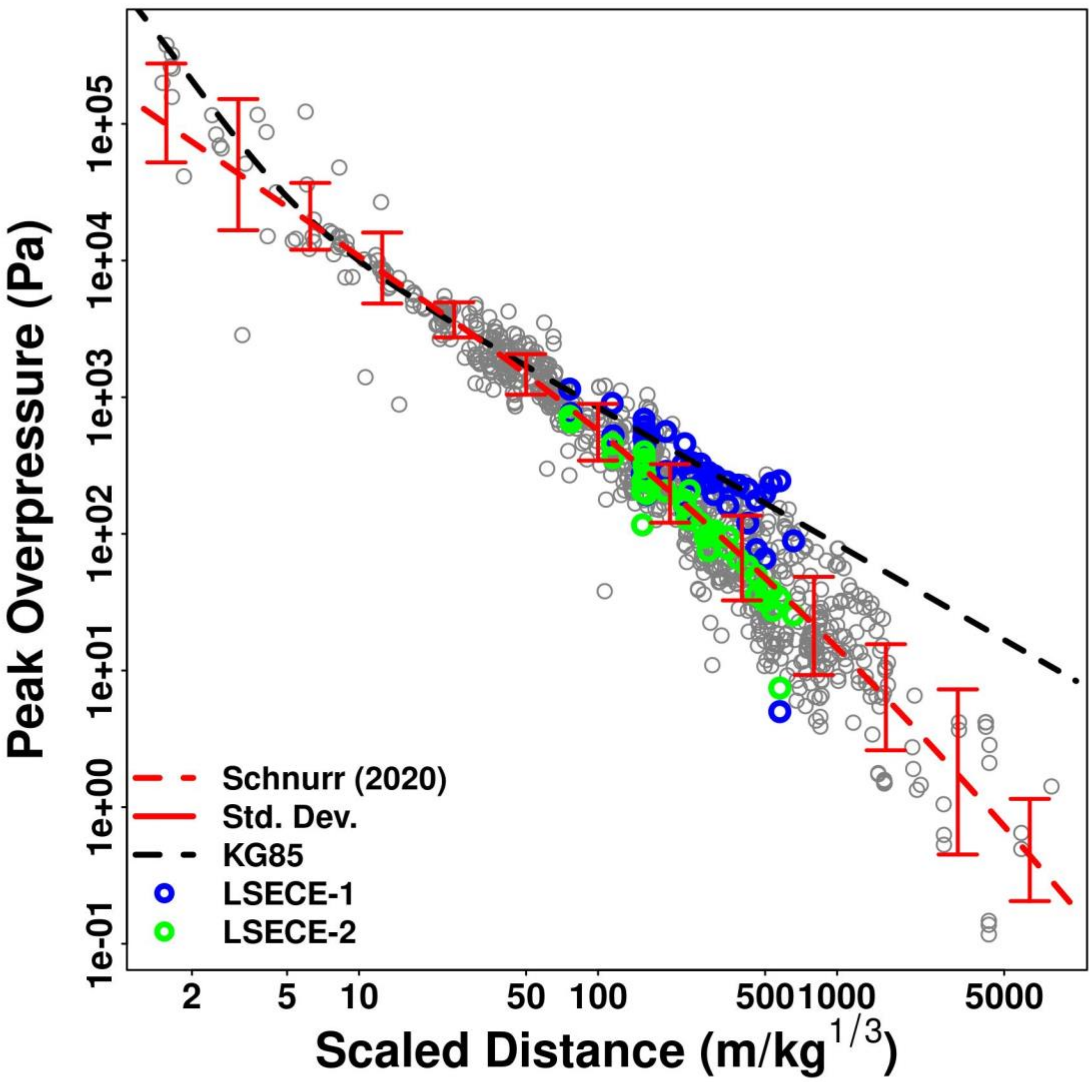

Figure 3. Peak overpressure measurements for LSECE. LSECE-1 (blue circles) and 2 (green circles) are compared with other dataset (gray circles) published by Schnurr et al. (2020). The peak amplitudes and distances are scaled for a 1kg TNT explosion on the surface. The red dashed line and vertical error bars denotes the mean and standard deviation of the other dataset. The black dashed line is a semi-empirical blast model published by Kinney and Graham (1985), which assumes propagation in a homogeneous atmosphere.

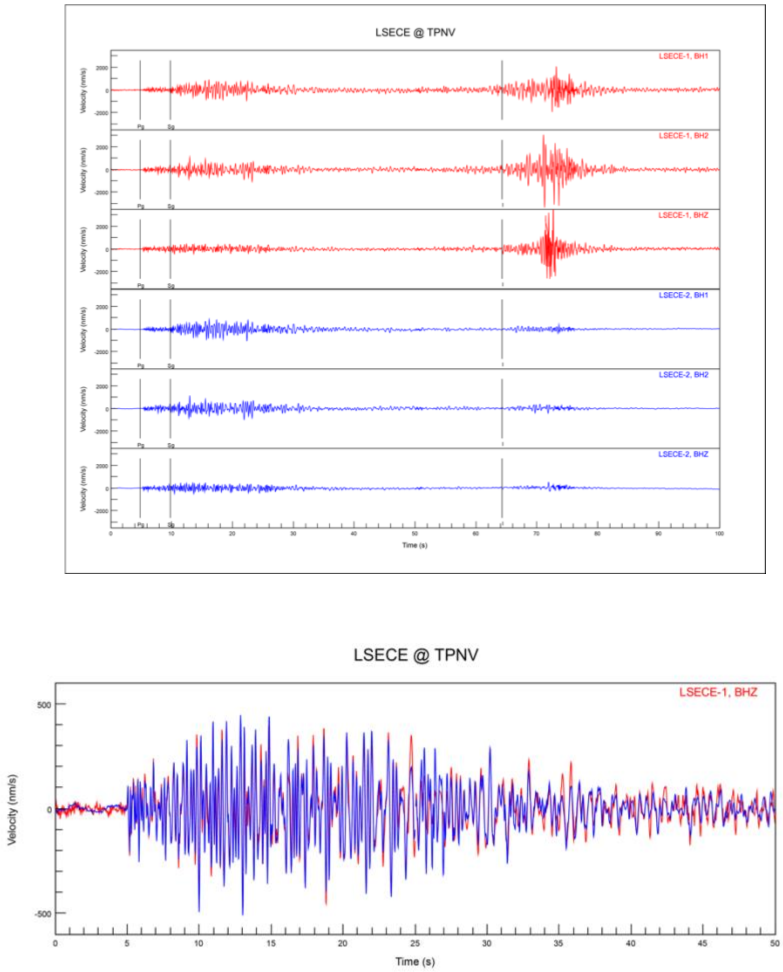

Figure 4. Seismic signals recorded for LSECE-1 and 2. Seismic phases and ground-coupled acoustic waves (following the seismic phases) are recorded on the seismometer (top). The Pg, Sg, and I labels mark the approximate arrivals of the P-wave, S-wave, and acoustic wave, respectively. The direct comparison of the seismic portion is shown on the bottom panel.

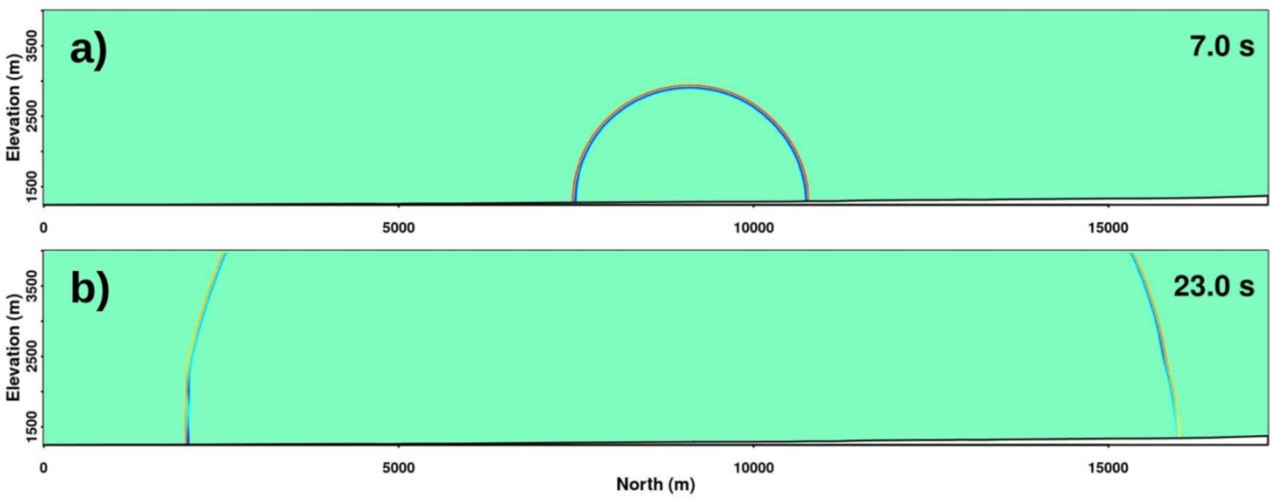

Figure 5. Finite-difference simulation images of acoustic wave propagation for LSECE-1. The images illustrate acoustic propagation on a vertical cross-section in the north-south direction from the source. a) Early wavefront development near the source 7 seconds after the detonation. The wavefront is characterized by spherical radiation. b) Wavefronts after 23 seconds of the detonation. The wave amplitudes are significantly different in the south and north directions. The high amplitude in the south is attributed to the waveguide observed in the radiosonde profiles (Figure 2).

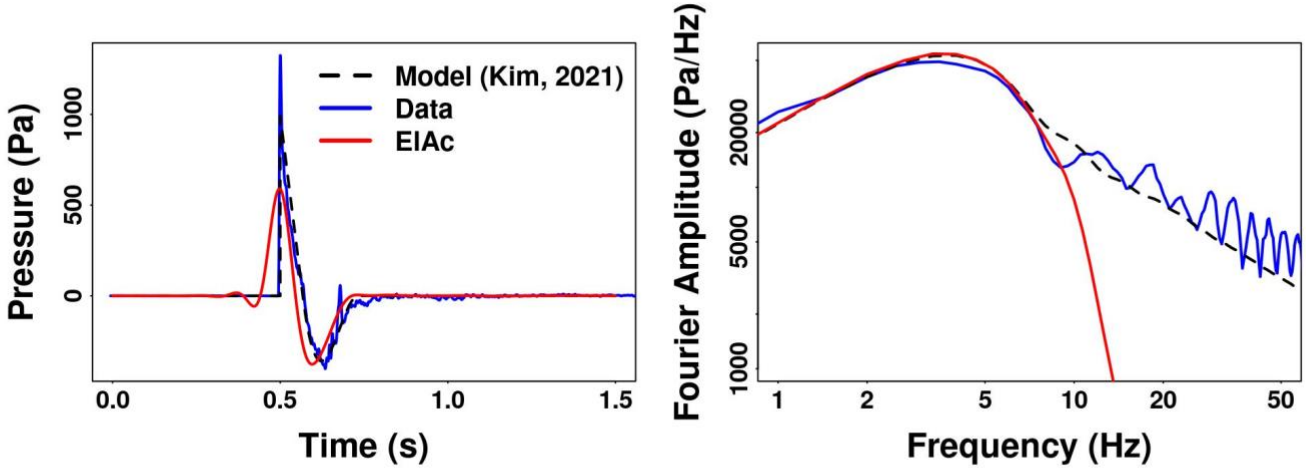

Figure 6. Waveform prediction for LSECE-1 in time (left) and frequency domain (right). The blue line is the observed signals at 1 km from the source to the south. The red line is the synthetic waveform predicted by the finite-difference simulation using the local weather data for background atmosphere. The black dashed line is the K21 model assuming homogeneous atmosphere. The data and predicted models are aligned with respect to their peak amplitudes for comparison. At this close distance, the empirical K21 model shows good agreement with the observation. Note that the finite-difference simulation result is band-limited. Below 10 Hz, the finite-difference model is also in good agreement with the observation.

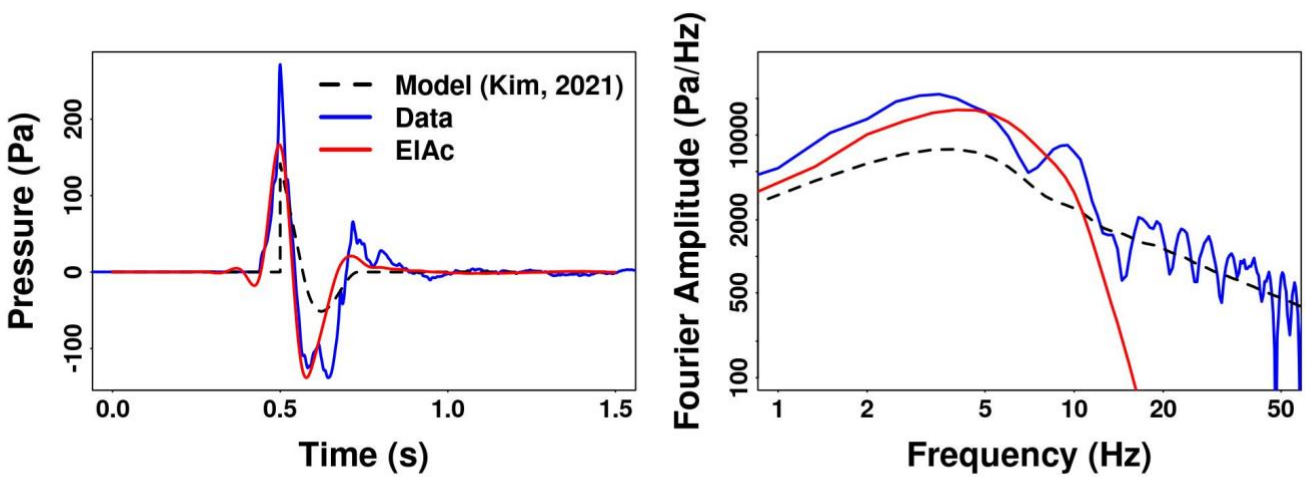

Figure 7. Waveform prediction for LSECE-1 at 7 km to the south. The blue, red, and black dashed lines are the observation, finite-difference model, and K21, respectively as for Figure 6. At this distance, the K21 model shows large prediction error due to unaccounted atmospheric propagation effects. However, the finite-difference model shows much better fit to the data, particularly below 10 Hz.

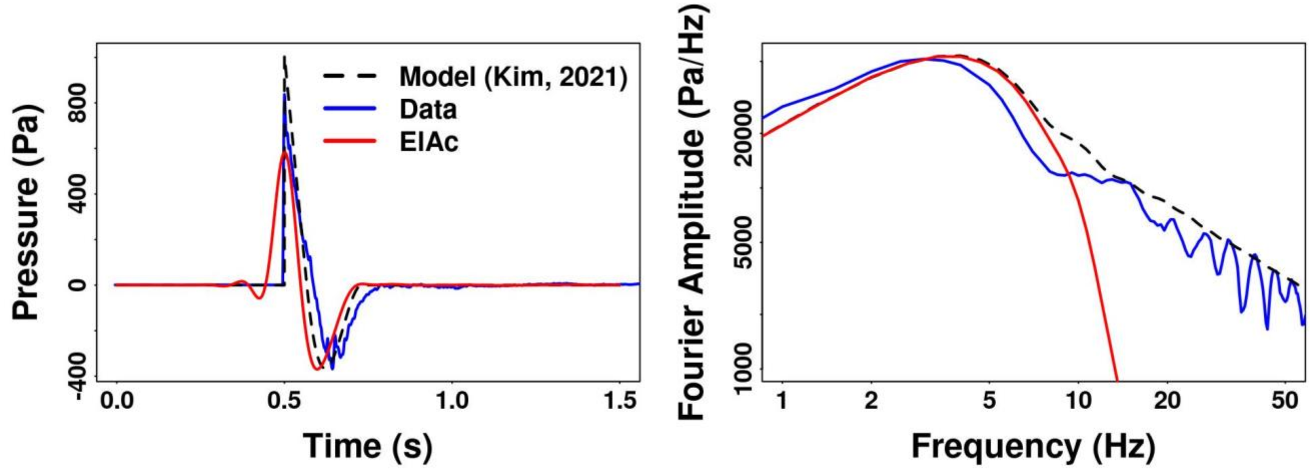

Figure 8. Waveform prediction for LSECE-2 at 1 km to the south. The blue, red, and black dashed lines are the observation, finite-difference model, and K21, respectively as for Figure 6. As in Figure 6, both K21 and finite-difference models show good agreement with the data at this distance, indicating insignificant weather impact on propagation.

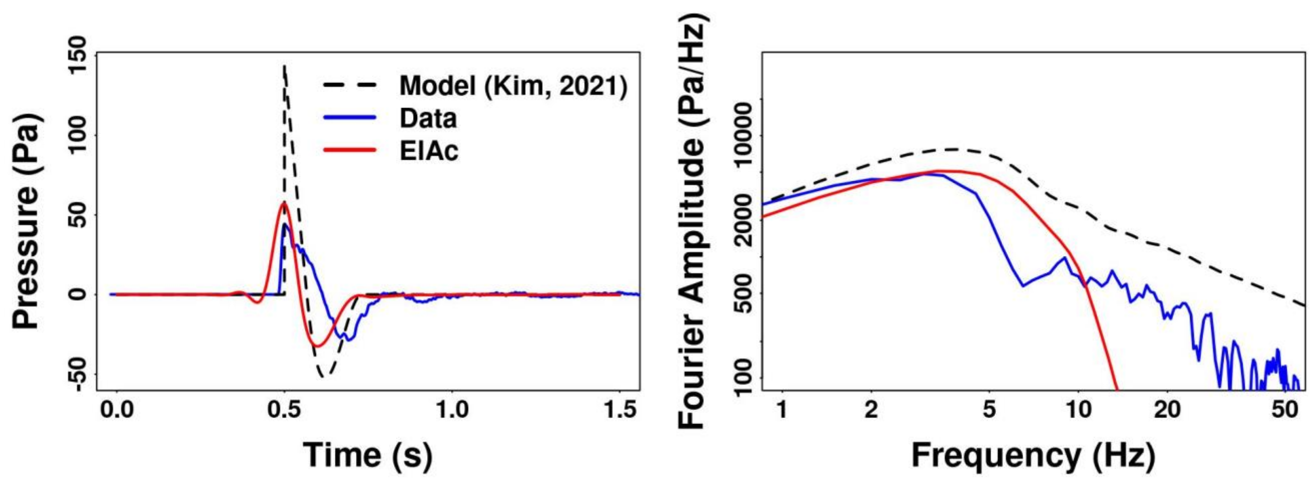

Figure 9. Waveform prediction for LSECE-2 at 7 km to the south. The blue, red, and black dashed lines are the observation, finite-difference model, and K21, respectively as for Figure 6. As for LSECE-1, finite-difference model show much better prediction than the K21 model.

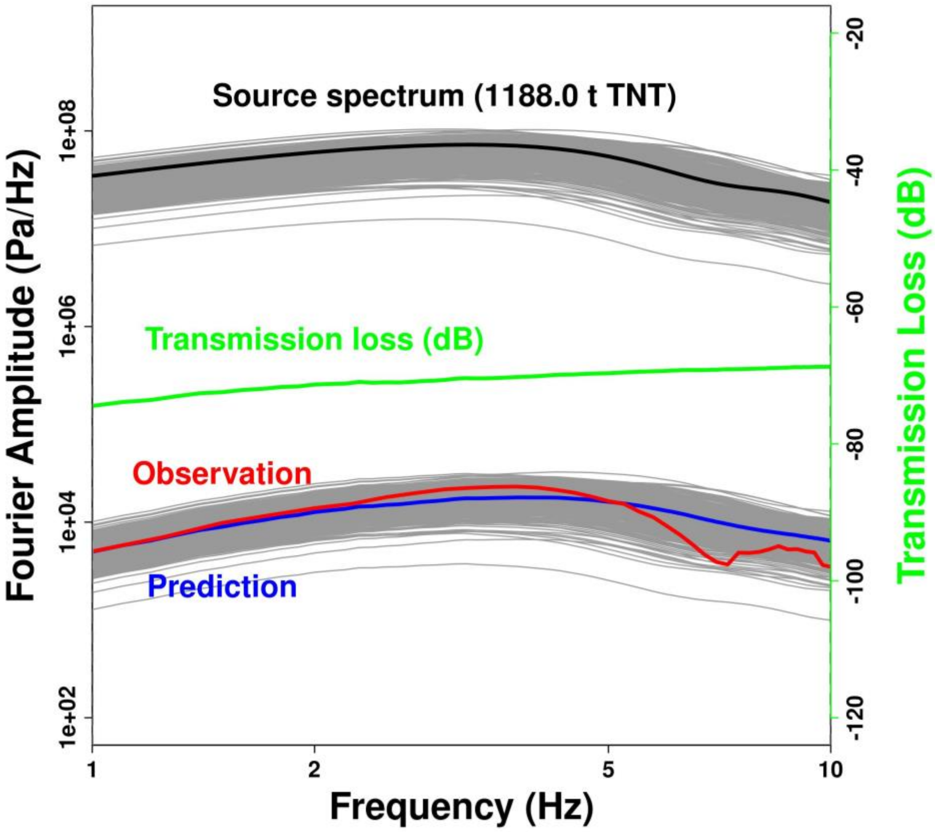

Figure 10. Acoustic signal prediction in the frequency domain. The source spectrum at a given yield (black line) is multiplied by the transmission loss (green line) to obtain frequency spectrum of prediction (blue) in comparison with the data (red). The K21 model provides the probability distribution of the source spectrum, leading to random realizations of possible sources (gray lines). Based on the source spectrum variation, a group of predictions (gray lines) are made for the observations.

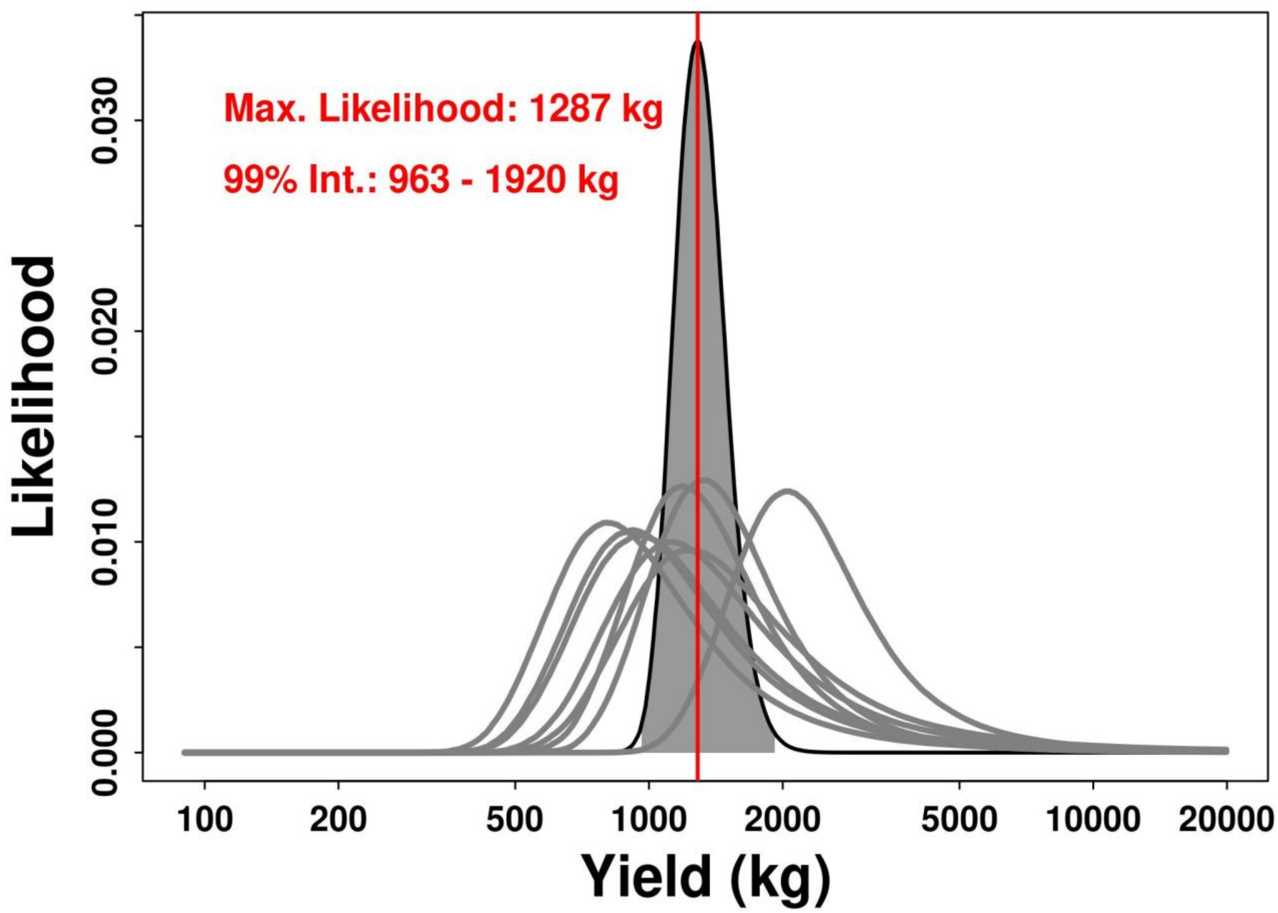

Figure 11. The probability distribution of the estimate yield for LSECE-1. The grey lines are distributions for individual stations, and the black line is the joint distribution made of the individual distributions. The 99% confidence interval was denoted by the shaded region.

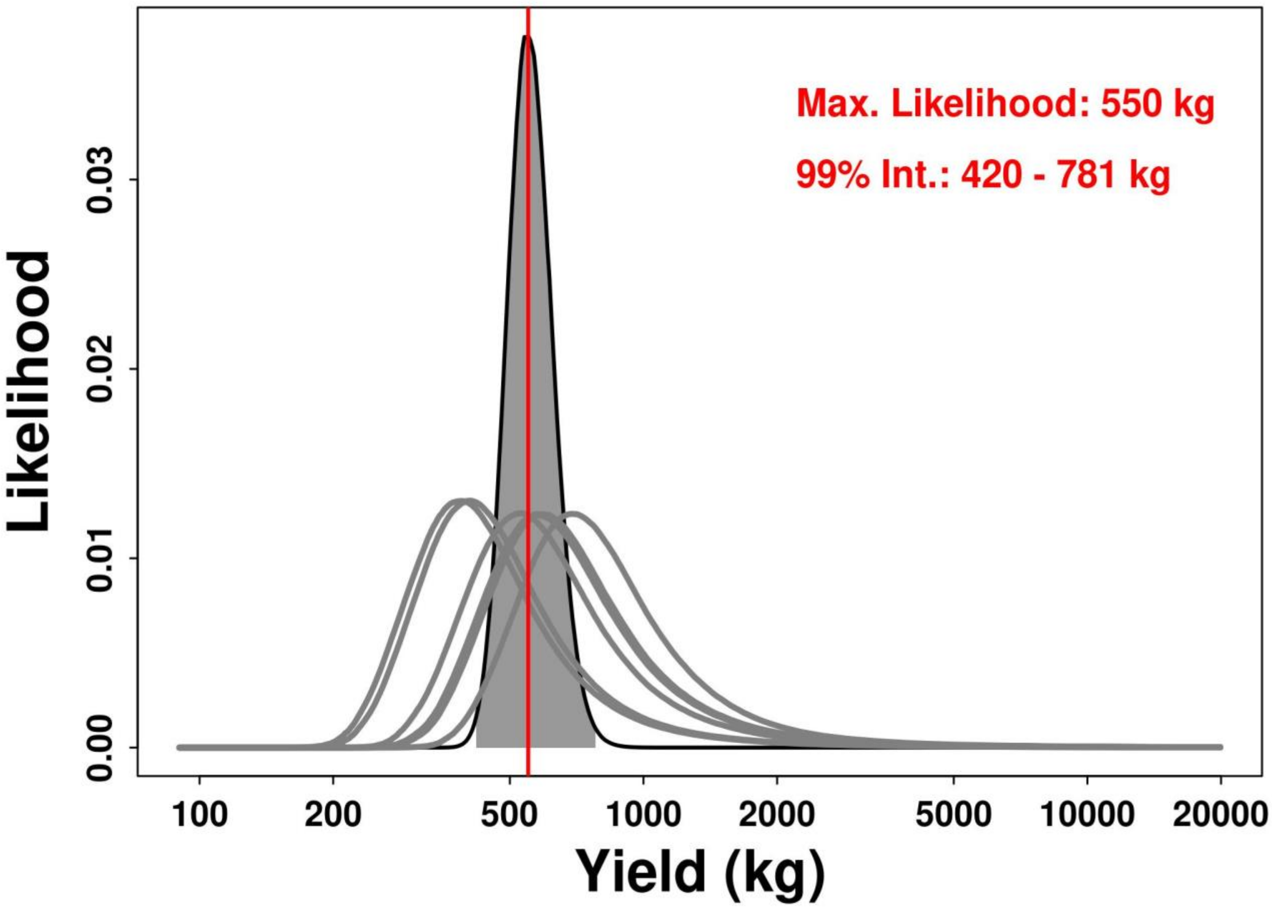

Figure 12. The probability distribution of the estimate yield for LSECE-2. The grey lines are distributions for individual stations, and the black line is the joint distribution as for Figure 11. The 99% confidence interval was denoted by the shaded region.

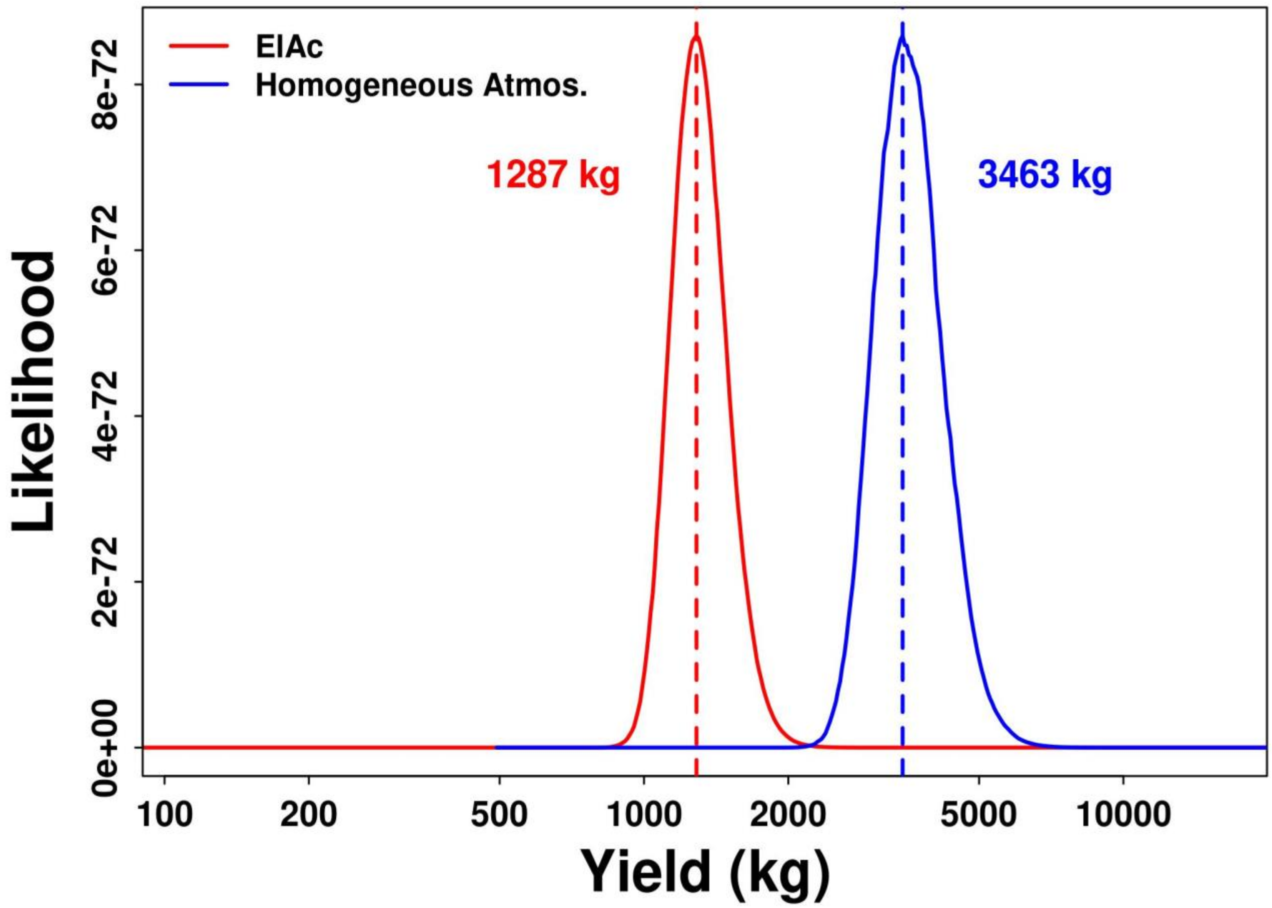

Figure 13. The comparison of estimated yields and probability distributions for LSECE-1. The distributions are obtained by the inversions with the finite-difference modeling (red) and K21 model with homogeneous atmosphere (blue). The maximum-likelihood yields are estimated as 1287 kg for the finite-difference model and 3463 kg for the K21 homogeneous model.

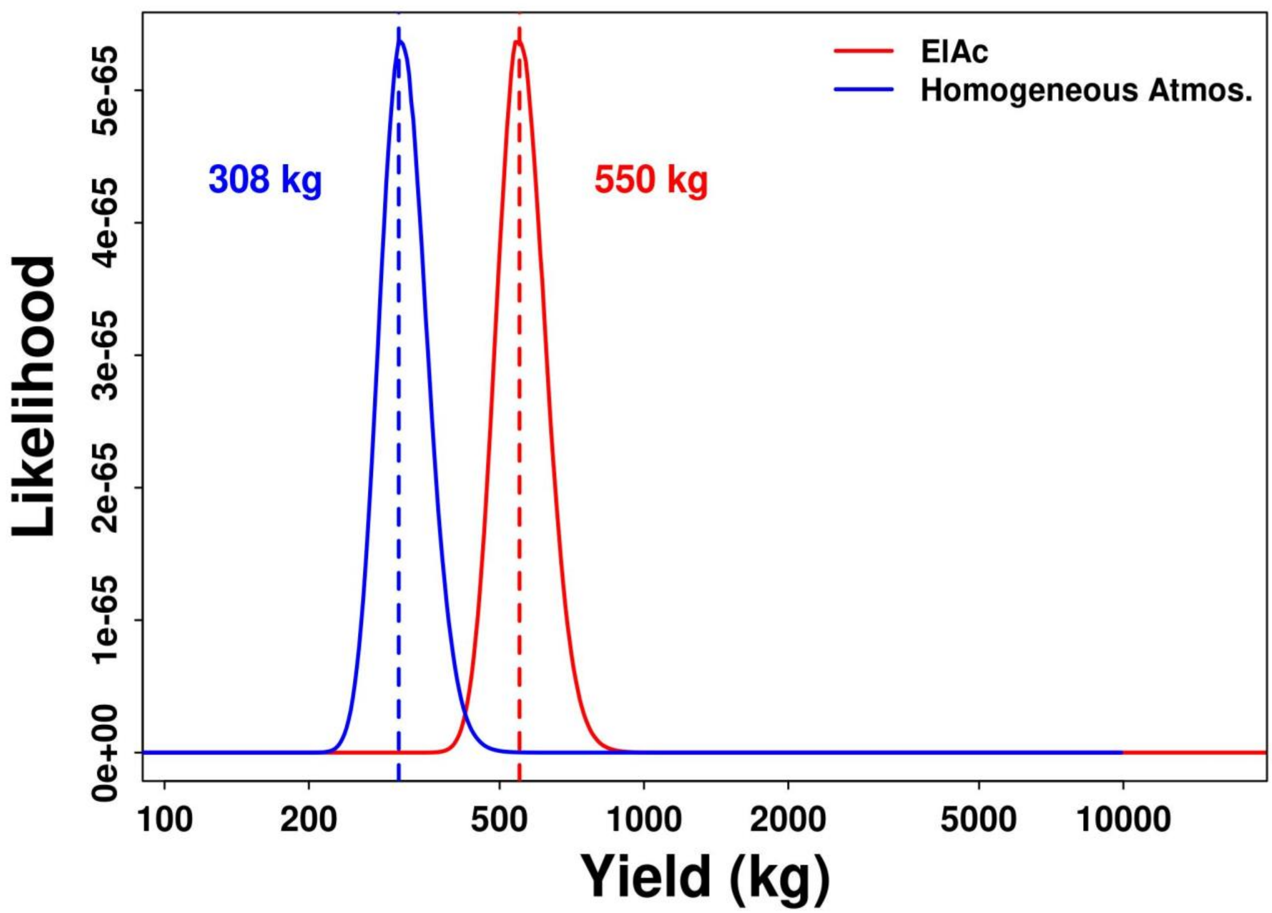

Figure 14. The comparison of estimated yields and probability distributions for LSECE-2. As for Figure 13, the red and blue lines are the distributions obtained by the finite-difference modeling (red) and K21 model with homogeneous atmosphere (blue). The maximum-likelihood yields are estimated as 550 kg for the finite-difference model and 308 kg for the K21 homogeneous model.

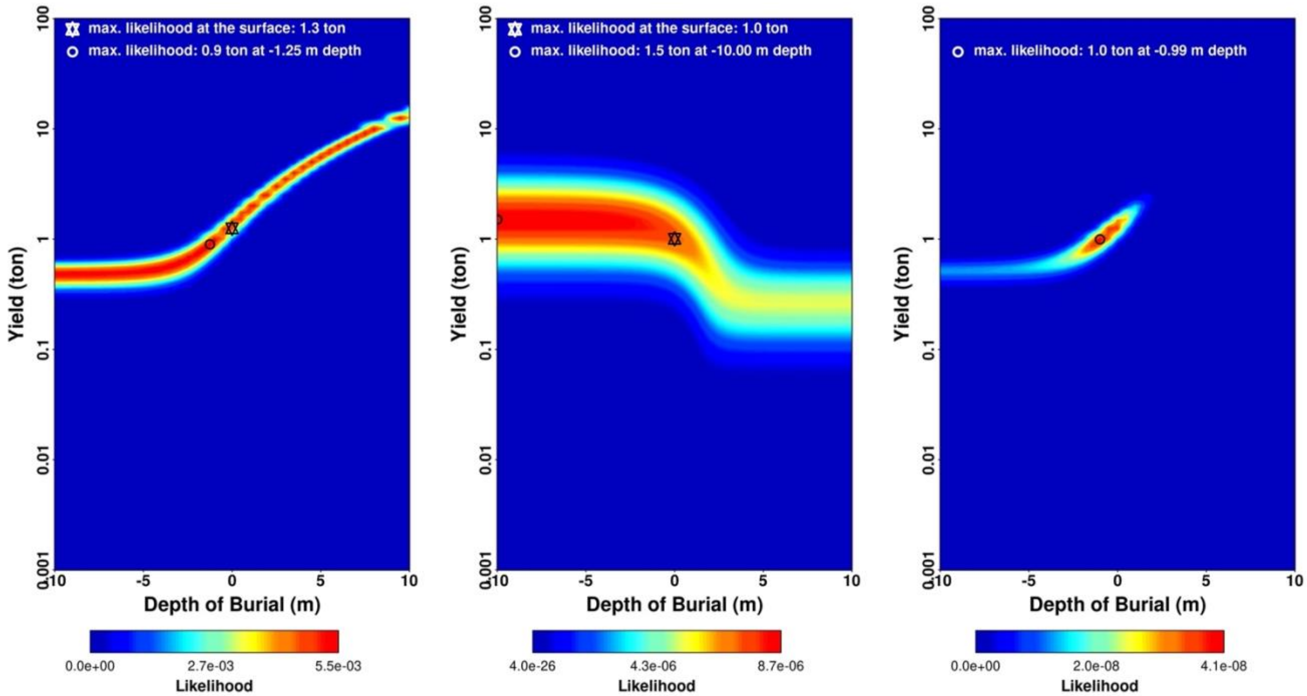

Figure 15. Likelihoods of explosion yields and depths for LSECE-1. Acoustic (left) and seismic (right) likelihoods are combined for the joint likelihood (right). The maximum likelihood yields assuming a surface explosion are denoted by the white star. The maximum likelihood yields without depth assumption are denoted by the white circle.

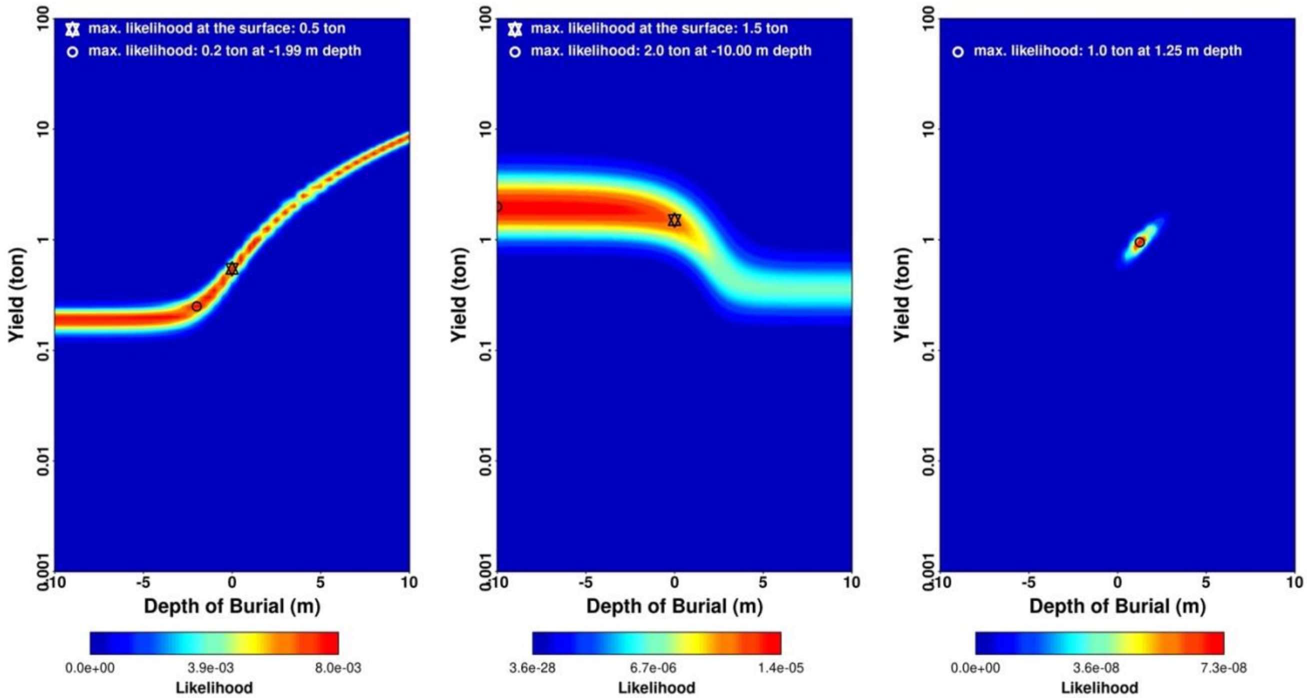

Figure 16. Likelihoods of explosion yields and depths for LSECE-2. Acoustic (left) and seismic (right) likelihoods are combined for the joint likelihood (right). As for Figure 15, the maximum likelihood yields with/without a priori depth are denoted by the white star and circle, respective